

Simulation of failure of air plasma sprayed thermal barrier coating due to interfacial and bulk cracks using surface-based cohesive interaction and extended finite element method

KYAW, Si <<http://orcid.org/0000-0001-8568-500X>>, JONES, I A and HYDE, T H

Available from Sheffield Hallam University Research Archive (SHURA) at:
<https://shura.shu.ac.uk/14264/>

This document is the Accepted Version [AM]

Citation:

KYAW, Si, JONES, I A and HYDE, T H (2016). Simulation of failure of air plasma sprayed thermal barrier coating due to interfacial and bulk cracks using surface-based cohesive interaction and extended finite element method. Journal of Strain Analysis for Engineering Design, 51 (2), 132-143. [Article]

Copyright and re-use policy

See <http://shura.shu.ac.uk/information.html>

Simulation of failure of air plasma sprayed thermal barrier coating due to interfacial and bulk cracks by using surface based cohesive interaction and extended finite element method

S.T. Kyaw*, I.A.Jones, T.H.Hyde

Faculty of Engineering, The University of Nottingham
University Park, Nottingham, NG7 2RD, UK

*Corresponding author email: si.kyaw@nottingham.ac.uk

Address: C03, ITRC building, University Park, University of Nottingham, NG7 2RD

Phone: +44-1159513811

Abstract

The present paper describes a method of predicting the failure of a thermal barrier coating system due to interfacial cracks and cracks within bulk coatings. The interfacial crack is modelled by applying cohesive interfaces where the thermally grown oxide is bonded to the ceramic thermal barrier coating. Initiation and propagation of arbitrary cracks within coatings are modelled using the extended finite element method. Two sets of parametric studies were carried out, concentrating on the effect of thickness of the oxide layer and that of initial cracks within the ceramic coating on the growth of coating cracks and the subsequent failures. These studies have shown that a thicker oxide layer creates higher tensile residual stresses during cooling from high temperature, leading to longer coating cracks. Initial cracks parallel to the oxide interface accelerate coating spallation and simulation of this process is presented in this paper. By contrast, segmented cracks prevent growth of parallel cracks which can lead to spallation.

Keywords: TBC, cohesive interaction, XFEM, crack growth, spallation

Nomenclature

$N_I(x)$ Conventional shape function, taking the value 1 at node I and 0 at all other nodes

a Half diagonal length of the impression

a_I Enriched degree of freedom for XFEM

b_I^a	Enriched degree of freedom for XFEM
c	Half of the crack length
D	Damage parameter for the traction-separation model
E	Young's modulus
f	Crack nucleation factor
$F_\alpha(x)$	Crack tip asymptotic function for XFEM enrichment
G_C	Critical strain energy release rate (also G_{IC} , G_{IIC})
G_{eq}	Equivalent critical strain energy release rate mixed-mode failure
G_I	Strain energy release rate for Mode I failure (also G_{II} and G_{III})
K_I^C	Fracture toughness of Mode I failure
m	Loading stiffness
P	maximum indentation load
\underline{T}	Traction stress at which damage initiation occurs
u_I	Degree of freedom for node I
β	phase angle for mixed mode failure
$\underline{\delta}$	Crack opening/separation at which damage initiation occurs
δ_z	Critical crack opening at $D = 1$
δ_{eff}	Effective critical crack opening for mixed mode failure
δ_n	Critical crack opening for Mode I failure
δ_{slip}	Critical crack opening for Mode II failure
ξ	Material constant in equation for calculating K_I^C

1 Introduction

A thermal barrier coating (TBC) system is usually made up of three layers: ceramic TBC, bond coat (BC) and thermally grown oxide (TGO) and the substrate. An air plasma sprayed (APS) TBC system will be considered here and this manufacturing method is commonly used for spraying TBCs onto components of land based engines. Unlike the electron beam physical vapour deposition (EBPVD) method, which is used in the aerospace industry, the APS method does not require the use of a vacuum during manufacturing, bringing down the investment cost for coating equipments. Nevertheless, it requires multiple passes of spraying to achieve the required coating thickness.

The growth of parallel cracks within the coating and interfacial delamination cracks can lead to failure of coating systems. The initiation of these cracks can be predicted based on simulated stress distributions within the system. While this type of prediction is reasonable for failure analysis, it does not take into account stress relaxation as a result of the growth of cracks. Here, the failure of air plasma spray (APS) TBC systems for gas turbines will be explored by implementing models for the crack growth mechanisms both at the coating interfaces and within the bulk coatings.

Stresses which are concentrated around the TGO interfaces at the end of a thermal cycle have been assumed to be the major cause of spallation of the TBC. Tensile stresses originate from the mismatch of strains between layers of the TBC system during the start up or the shutdown of engines. When these stresses exceed the fracture strengths of the TBC layers or the TGO interfaces, they create cracks within the bulk layers and weaken the TGO interfaces by creating delamination cracks. The fracture toughness of the TGO interfaces and of the TBC layers determine the propagation of those cracks and of the overall failure mechanism (ductile or brittle) of TBC system.

Failures of TBC systems based on cracks created within the TBC and the TGO layers have been investigated experimentally by various researchers [1, 2]. Naumenko et al. [2] observed that failure of the APS TBC system mainly occurs within the TBC layer near the TGO/TBC interface because a significant amount of TBC remains attached to the substrate after failure, compared to EBPVD coating systems.

Delamination and spallation failures of TBC systems have been simulated using cohesive bonds with predefined crack paths [3-5] but these models are unable to predict arbitrary crack propagation within the bulk coatings as the crack paths are defined at the pre-processing stage. Although an iterative crack propagation scheme as presented in [6] can be used for modelling arbitrary propagations of cracks, excessive re-meshing around the crack

tip is required, and it is therefore computationally expensive especially for 3D models. Arbitrary crack propagation has been modelled for EBPVD systems in [7, 8] but the study does not implement cohesive interface for possible growth of interfacial cracks and delamination.

In this paper, the extended FE method (XFEM) is applied to the simulation of arbitrary crack propagation within the TBC and the TGO while a cohesive interaction is applied at the TGO/TBC interface to investigate the degradation of interface bonding. Furthermore, initial cracks and discontinuities within the TBC are also implemented in the model and their influences on TBC spallation are studied. Initial cracks could sometimes be deliberately introduced to the system using proprietary spraying processes such as the solution-precursor plasma sprayed process (SPPS) as explained in [9] for better strain tolerance.

2 Geometry and boundary conditions

Modelling has taken place regarding the initiation and propagation of cracks within the TBC system when it is cooled down from the operating temperature (1000°C) to 20°C. The TBC model consists of a nickel based superalloy cylinder with an inner (R_i) and an outer radius (R_o) of 3.2mm and 6.2mm respectively. The BC and the TBC with respective thicknesses of 100 μm and 200 μm are assumed to be coated onto the cylindrical substrate. The dimensions of the TGO interface have been taken as a wavelength of 48 μm and an amplitude of 6 μm ; these values are within the range of the typical TGO interface as measured in [10]. The current TBC model does not take account of out of plane geometry variations of complex TGO interfaces and relevant stress developments as shown in [11]. Geometries of the TBC system are shown in Fig. 1 (i) and (ii). Only one half of a period of a sinusoidal interface is used as FE unit cell as shown in Fig. 1 (i). Mesh and boundary conditions for a unit cell are illustrated in Fig. 1 (iii). Periodicity of a unit cell and symmetry boundary conditions are applied. Although generalised plane strain elements (CPEG4) are more suitable for constructing a 2D representation of a coated cylinder with prismatic surface features and of a finite length, the commercially available XFEM enrichment scheme in Abaqus [12] is not formulated for CPEG4. Therefore, a specially-developed user defined element (UEL) [12] was required. For simplicity, a plane strain element (CPE4) was used instead by assuming the cylinder is constrained against axial expansion or contraction. Elements with the full integration scheme for displacement based FEA tend to overestimate the element stiffness matrix as a result of shear locking [13]. Hence, a reduced integration

scheme with fewer Gauss (integration) points is advised for such simulations and it is therefore chosen for the current problem.

The TBC system is assumed to be defect-free during the pre-processing stage for the first part of analysis. Initial TBC cracks were implemented in the second part of the analysis in order to understand their influences on spallation. Two types of APS TBC cracks were considered for implementation at the pre-processing stage: cracks which originate from the intersplat boundaries, which are parallel to the TGO interface (parallel cracks), and cracks that are perpendicular to the interface (segmented cracks) as shown in Fig. 2 (i) and (ii) respectively. The formation of cracks is driven by maximum principal stresses of the TBC systems under thermal cyclic load.

Various researchers [14-16] have explored the relationship between the failure of the TBC system and the thickness of the TGO layer. To observe the relationship between crack growth and TGO thickness, parametric studies were carried out with different TGO thicknesses varied from 1 to 4 μm while keeping the aspect ratio the same as for the sinusoidal TGO interface for the initially crack-free model. The TGO thickness, for the model with initial defects, is set to 4 μm , which is assumed as the critical TGO thickness for the spallation, to simulate the final spallation of the TBC. The TBC system is considered to be stress-free at the end of the steady state due to the stress relaxation within the BC in accordance with the assumptions made by Rösler [17].

XFEM enrichment was applied to the TGO and the TBC layers based on the principal stress criterion. The adhesion between the TGO and the TBC layer and subsequent degradation of the interface from interfacial crack opening is modelled by using the cohesive interaction method [12] (CIM). The CIM is only applied to the TGO/TBC interface since it has been shown experimentally [2] that spallation of the TBC in the vicinity of the TGO is most common for APS TBCs.

3 Crack growth modelling using XFEM

Until recently, crack nucleation and propagation have been modelled within Abaqus using virtual crack closure or cohesive methods. These methods allow crack growth along a predefined path following the element boundaries. This has limited the potential of modelling arbitrary crack growth within the model. Moreover, computationally demanding mesh optimisation is required around the crack tip where stress concentrates. By using a displacement interpolation scheme [12] as shown in Eq (1), XFEM can model initiation of cracks without specifying predefined crack paths. It was introduced by Belytschko and Black

[18] by further enhancing the partition of unity method introduced by Melenk and Babuska [19].

$$\mathbf{u}^h(\mathbf{x}) = \sum_{I \in N} N_I(\mathbf{x}) \left[\mathbf{u}_I + [\text{sgn}(\mathbf{x}) \mathbf{a}_I]_{I \in N_H} + \left[\sum_{\alpha=1}^{N_{\text{tip}}} F_{\alpha}(\mathbf{x}) \mathbf{b}_I^{\alpha} \right]_{I \in N_{\text{tip}}} \right] \quad (1)$$

where $N_I(\mathbf{x})$ is a conventional shape function used in elements, regardless of whether XFEM enrichment is used. \mathbf{u}_I represents the degrees of freedom (dof) of nodes for the FE calculations within ordinary isoparametric elements, while \mathbf{a}_I and \mathbf{b}_I^{α} are enriched dof for the implementation of discontinuities within the elements. $\text{sgn}(\mathbf{x})$ is a Heaviside distribution. N_H are nodes belonging to the elements cut by a crack. N_{tip} are nodes belonging to the element within which a crack tip lies. $F_{\alpha}(\mathbf{x})$ is a crack tip asymptotic function. More details for the XFEM can be found in [20].

For propagating cracks, the traction-separation model (explained in Section 4) is applied using phantom nodes. Phantom nodes are superimposed onto the nodes of the elements through which the crack has passed. These phantom nodes at opposite sides of the crack will be separated causing opening of the crack face as the loading is applied. The magnitude of the separation of the crack surface before the complete failure is governed by the fracture toughness of the material. For propagating cracks, the crack tip asymptotic singularity is not considered. This means that a crack only initiates when all nodal values (stress or strain) for the element are higher than user-defined critical values, and the crack tip always lies at the element boundary.

In terms of engineering applications, XFEM can be used to predict arbitrary solution-dependent crack initiation and propagation within structures under loading. It can be used in parallel with cohesive failure models. Here, it is used to model crack propagation within the TBC and TGO in conjunction with the CIM model for the propagation of a delaminating crack at the TGO/TBC interface.

4 Traction-separation damage model

A linear traction-separation law [21] as shown in Fig. 3 was applied as a damage model for both cohesive nodes of the TGO/TBC interface and XFEM enriched elements. The model has been applied extensively in [5, 7, 8] to simulate either interfacial cracks or cracks within coating layers. k from Fig. 3 is the cohesive stiffness and it is the ratio of the traction

stress (\underline{T}) and separation ($\underline{\delta}$) at which damage initiation occurs. Damage or crack initiation can be determined by either a critical principal stress/strain or a critical separation criterion. Stresses between the crack surfaces reduce while the cohesive interface or the crack plane is separating during degradation. If unloading is applied at point Y (refer to Fig. 3), the cohesive stiffness is reduced to $(1-D) \times k$ for the next loading step. D is the damage parameter and it can be derived as follows.

D is zero during the elastic loading region (OX) and if the unloading occurs at this region both traction and crack separation should go back to zero. Damage initiates at point X where D is 0 and final failure point is Z where D is 1. To illustrate this, the damage parameter is derived for unloading at point Y as shown in Fig. 4. The loading stiffness (m) after unloading at point Y will be

$$m = (1 - D) \left(T^u / \delta_y \right) \quad (2)$$

However, $\left(T^u / \delta_y \right)$ is the stiffness of the undamaged crack (k). Hence m can be expressed in terms of k . T^u is the stress when there is no cohesive damage whereas T^d is the actual traction stress with cohesive damage.

The damage parameter D can be related to the crack separation distances. The slope m is written again as

$$m = YR / OR \quad (3)$$

Since ZQX and ZRY form a pair of similar triangles, YR can be written as

$$YR = QX \times \frac{ZR}{ZQ} = T^u \times \frac{(\delta_z - \delta_y)}{(\delta_z - \underline{\delta})} \quad (4)$$

Substituting Eq (2) & (4) into (3),

$$T^u \times \frac{(\delta_z - \delta_y)}{(\delta_z - \underline{\delta})} = \delta_y (1 - D) \left(T^u / \delta_y \right) \quad (5)$$

By simplifying Eq (5), the damage parameter can be related to crack opening displacement as

$$D = \frac{\delta_z (\delta_y - \underline{\delta})}{\delta_y (\delta_z - \underline{\delta})} \quad (6)$$

Final failure occurs when the strain energy release rate due to the crack opening is higher than the critical strain energy release rate (G_C). The strain energy release rate can be calculated as the area under the traction-separation graph (Fig. 3). The type of failure largely

depends on the value of G_C ; high and low G_C are related to the ductile and brittle failure respectively.

Critical crack opening (δ_z) depends on the fracture stress (\underline{T}) and fracture toughness (κ_I^C) and relationship for Mode I failure is shown in Eq (7).

$$\delta_z = \frac{2 (\kappa_I^C)^2}{E \underline{T}} \quad (7)$$

5 Traction-separation damage model for mixed mode loading

If a shear mode of failure is taken into account, the effective critical separation (δ_{eff}) can be expressed using normal crack opening (δ_n) and tangential crack opening (δ_{slip}) as shown in Eq (8). This effective separation can be used to define failure criterion as an alternative stress based criteria as follows. For mixed mode failure, a quadratic stress or strain criterion can be used for damage initiation in traction-separation model [12] and the former is used here to derive mixed mode failure parameters. The crack nucleates when the parameter (f) as shown in Eq (9) becomes unity.

$$\delta_{\text{eff}} = \sqrt{\delta_n^2 + \delta_{\text{slip}}^2} \quad (8)$$

$$f = \left(\frac{\langle \sigma \rangle}{\sigma_c} \right)^2 + \left(\frac{\tau}{\tau_c} \right)^2 \quad (9)$$

where σ and τ are nodal direct and shear stresses and σ_c and τ_c are critical direct and shear stresses. The Macaulay bracket means only tensile direct stress is considered for crack initiation. If $\tan \beta = \frac{\tau}{\langle \sigma \rangle}$, then the effective traction stress for damage initiation can be

described as in Eq (10), where β is the phase angle for mixed mode failure.

$$\underline{T} = \sigma_c \left(\cos^2 \beta + \frac{\sigma_c^2}{\tau_c^2} \sin^2 \beta \right)^{-0.5} \quad (10)$$

For mixed mode damage evolution, the critical energy G_C is the equivalent critical strain energy release rate (G_{eq}). This can be calculated in various ways [12]; a B-K (Benzeggagh and Kenane) law for G_{eq} is shown in Eq (11) as an example.

$$G_{\text{eq}} = G_{\text{IC}} + (G_{\text{IIC}} - G_{\text{IC}}) \left(\frac{G_{\text{II}} + G_{\text{III}}}{G_{\text{I}} + G_{\text{II}} + G_{\text{III}}} \right)^n \quad (11)$$

where G_{IC} and G_{IIC} are critical strain energy release rates of direct and shear modes of failure respectively and G_I , G_{II} and G_{III} are energy release rate for a direct and two shear modes of failure respectively. n is a constant power, which is usually determined empirically.

Currently, it is assumed that the initiation and evolution of damage are independent of failure mode, due to lack of experimental data. Once experimental data for the shear strengths and mode dependent energy release rates of the coatings are available in future, they can be implemented in the mixed-mode failure model as shown by the framework above.

6 Material properties

6.1 Elastic and thermal properties

To model time dependent material properties of a complex TBC system, a user defined material subroutine (UMAT) is required [22]. Due to current limitations of the XFEM code implemented within Abaqus [12], it is not possible to couple UMAT with XFEM code. A more complicated user defined element (UEL) is required for this purpose. As a first attempt, the coating layers are currently considered to be elastic during the cooling stage and the system is also assumed to be stress-free at the beginning of the cooling stage. Elastic and thermal properties for the substrate, the TGO and the coating layers are given in Table 1. The system used for the study is an APS TBC system. It includes IN-738LC superalloy substrate, yttria stabilised zirconia (YSZ) ceramic coating, beta (NiAl) - gamma (Ni) BC and alumina (Al_2O_3) TGO. Please note that elastic and CTE of TBC are measured at room temperature. However studies[23-27] have shown that sintering at high temperature could modify the elastic modulus significantly and hence either empirical sintering model [22] or physical models [28] should be considered for further studies.

Despite the simplifications made in this study, significant research [29-31] has showed the effects of dilational strain, due to growth of an oxide layer during the steady state at high temperatures, on residual stress state within TBC systems. These stresses are further distributed due to creep relaxation of bond coat as demonstrated in [32-35]. Hence, further work is expected to couple the current analysis with thermo-mechanical analysis of TBC system with time dependent material properties and oxide growth like models in [22, 34] using the user defined element (UEL) feature within Abaqus [12].

6.2 Tensile strengths of coatings

To apply the traction-separation law, the maximum stress and cohesive interface stiffness for damage initiation and the critical strain energy release rate for damage evolution and failure have to be defined. Tensile strength was taken as the maximum stress for damage initiation by assuming that both the TGO and TBC are brittle with no yielding at the point of failure. Tensile strength of the TGO is 260MPa as reported by Munro [36]. The strength does not vary significantly for the temperature range between 20°C and 1000°C although it falls linearly to 10MPa between 1000°C and 1400°C [36]. It is assumed that TGO formed within the TBC system is comparable to bulk alumina (mass fraction of $\text{Al}_2\text{O}_3 \geq 0.995$ and a nominal grain size of 5 μm) used for experimental testing in [36]. The fracture stress of the YSZ TBC is largely dependent on its yttria content as demonstrated in [37]. It was observed that at a high concentration of yttria, the tensile strength is almost equal to the flexural strength. Since no reliable temperature dependent tensile strengths are available, the temperature dependent flexural strengths of YSZ with 6.5 mol% of yttria in [38] are taken as the fracture strength of the TBC. The strength of the sintered YSZ varies from 150 MPa to 50MPa between 20°C to 1000°C. Please note that the specimens used for the experiments in [36, 38] are made up of bulk coating materials whose dimensions are much larger than actual coating layers. The tensile strength of coatings could be size-dependent and it should be investigated further.

6.3 Interfacial tensile strength

Coating failure is strongly dependent on the adhesion strength of the interface under tensile loading. Various techniques have been proposed to estimate the tensile adhesion strength of the TBC. The most common standardised methods are DIN 50160 and ASTM D7234-05 both of which are tensile pull tests. These have been applied in [39, 40] to obtain TBC bond strength. An experiment following the DIN 50160 standard is shown in Fig. 5. It is doubtful that the measured bond strength represents the actual adhesion strength at the coating interface as the measured values [39, 41] are much lower than analytically or numerically predicted mismatch stresses at the interface. To obtain reliable strength data from a pull test, the bonding strength of the epoxy has to be stronger than that of the coating in order to avoid failure at the epoxy interface. Moreover, because of the porous nature of APS TBC, the adhesive can seep into the coating and this might alter the strength of the coating/metal interface. Finally, at the point of coating failure, the ratio of failure load to coated area is taken as the bond strength without considering the area of any initial flaws.

Therefore, the predicted bond strengths from pull tests such as the one in [39] are much lower than maximum out-of-plane tensile stresses (normal to the coating interface) simulated using FE models.

An alternative method for bond strength, which is based on experimental spallation tests and the FE method, is proposed as follows. It is assumed that the coating delaminates when the mismatch stress, due to cooling, exceeds the critical stress as explained in [26]. Experimentally, the critical thermal load for delamination can be obtained by applying different thermal cycles to the TBC system. According to data from spallation tests [42], delamination occurs after cooling down from heating at 1000°C for 1050h. When the same thermal cycle was applied to the FE model of the TBC system [22], the maximum tensile out-of-plane stress at the TGO/TBC interface is found to be 196.5MPa at the end of cooling. This stress is taken as the delamination strength of the interface.

6.4 Interfacial cohesive stiffness

Unlike physical properties (e.g. the tensile strength or toughness of materials), the cohesive stiffness for traction-separation model is an assumed property without a direct physical interpretation. Some researchers investigating adhesive joints [43] have suggested the use of a stiffness value which is equal to the ratio of the modulus of the adhesive to its thickness. However, the physical thickness of the adhesive has no relevance to the case of a cohesive bond as in the model applied here. Therefore, a sensitivity study was carried out to obtain a useful interface cohesive stiffness. This is chosen to give values of out-of-plane stress at the cohesive interface, within the linear elastic region, close to the stress values predicted from the model with completely tied interfaces. The value of traction stress for damage initiation at the TGO/TBC interface is assumed to be 3 GPa to ensure the mismatch stresses will not initiate delamination cracks and affect the stress distribution. Cohesive stiffnesses ranging from 1.5×10^8 to 1.5×10^{11} MPa/mm were applied at the TGO/TBC interface within the sensitivity study.

Maximum difference between out-of-plane stresses at the TGO/TBC interface given by a cohesive interface model and by the model with a tied interface is plotted for different cohesive stiffnesses as shown in Fig. 6. For a cohesive stiffness of 1.5×10^{11} MPa/mm, the difference is less than 1.5% and this value was therefore chosen as the cohesive interface stiffness for the studies carried out here. Although a larger cohesive stiffness can be chosen, an overly stiff interface will need a very small crack opening (for the current case the opening

is less than 1.31×10^{-10} mm for a cohesive stiffness of 1.5×10^{12} MPa/mm) before the damage starts. This can lead to numerical instability.

6.5 Critical strain energies and fracture toughness

The critical strain energy release rate can be related to the bulk/interfacial fracture toughness (K_I^C) and modulus (E) as $G_C = (K_I^C)^2 / E$ for plane strain Mode I failure. The fracture toughness values for a TGO film (thickness = 0.38 μ m) and bulk TBC (thickness = 1mm) were measured by Stollberg, et al. [44] using the nanoindentation method. The relationship between nanoindentation test data and fracture toughness value can be shown by Eq (12). The corresponding values are 2.22 ± 0.31 and 1.3 ± 0.29 $MPa\sqrt{m}$. Yamazaki *et al.* [45] investigated the TGO/TBC interface toughness and estimated it to be around 3.5 $MPa\sqrt{m}$. In the absence of the physical elastic modulus for the TGO/TBC interface, the apparent modulus of the interface acquired from the load-depth indentation curve according to ISO 14577 is used by Yamazaki *et al.* [45]. The modulus is obtained by equating fracture toughness measured by the nanoindentation technique to the value measured from a 4 point bend test [45]:

$$K_I^C = \xi \frac{a}{\sqrt{c^3}} \sqrt{P \cdot E} \quad (12)$$

where ξ is a constant, E is the elastic modulus or apparent elastic modulus for interfacial toughness, a is half diagonal length of the impression, P is maximum indentation load and c is half of the crack length.

7 Results and discussion

7.1 Parametric study of the influence of TGO thickness on crack growth within bulk coatings

For initially defect-free systems, after cooling down from 1000°C to 20°C, principal stresses within the TBC systems for different TGO thicknesses are presented in Fig. 7. The stress contours are significantly different from those relating to the crack-free models [14, 34, 46], which show stress concentrations at the peak and valley regions of the TGO interfaces. However, for the current models, stresses at the peak region of TBC/TGO interface are relaxed by crack formations and stresses are found to be concentrated at the flank of the interface instead. The changes in crack propagation direction for the TBC cracks are not as

significant as the changes in direction for TGO cracks, which are growing towards the TGO/TBC interface. Thicker TGOs can lead to higher mismatch stresses within the TBC system[14], which cause propagation of longer cracks. From the current study, the TBC crack propagates completely through the periodicity plane AB of the model when the TGO is thicker than 2 μ m. Therefore, coalescence of cracks within the TBC and the spallation of the TBC are expected when the TGO becomes thicker due to oxidation of the system at high temperature.

As shown in Fig. 7, there are multiple regions with stresses which are higher than the tensile strength of the coatings, and these stresses can cause initiation of further cracks. However, in this case, new cracks are not generated due to the limitations in the XFEM enrichment within Abaqus [12]. Formation of new cracks is not allowed in the vicinity of the existing crack until the complete separation of the existing crack face occurs. This could be because formation of multiple cracks within an element is not currently supported by Abaqus. In other words, XFEM is not suitable for modelling failure caused by multiple cracks which nucleate simultaneously. As seen from the damage parameter contours for XFEM cracks shown in Fig. 8, the existing cracks have some regions with damage parameters less than 1. This prevents the initiation of new cracks near the regions of the existing cracks.

7.2 Parametric study of influence of TGO thickness on crack growth at the TGO/TBC interface

The damage status of a delamination crack at the interface can be studied by monitoring the contact opening variable within Abaqus. For mixed-mode failure, the effective opening (δ_{eff}) can be calculated from direct (COPEN, δ_n) and shear crack opening (CSLIP, δ_{slip}) variables as shown in Eq (8). The crack opens when δ_n or δ_{slip} is higher than $\underline{\delta}$ and the complete failure occurs when δ_{eff} reaches the critical separation (δ_z) as shown in

Fig. 3. For this case, ($\underline{\delta}$) and δ_z are 1.31×10^{-09} mm and 1.597×10^{-3} mm respectively. δ_n and effective separations along the TGO/TBC interfaces are plotted for systems with different TGO thicknesses as shown in Fig. 9 & Fig. 10 respectively. Generally, tangential separations are around half an order to an order of magnitude higher than normal separations (Fig. 9 & Fig. 10). None of the models show a completely delaminated interface while contact separations in both directions are higher for thicker TGOs. However, the separations for the model with 4 μ m TGO are lower compared to the values from the system with 3 μ m TGO because of higher stress relaxation at the interface for 4 μ m TGO model from the formation of multiple cracks (Fig. 8).

7.3 Influence of initial parallel TBC cracks on crack growth within the TBC system

For the system with an initial parallel crack, the existing crack has little effect on the initiation of the TGO crack and its propagation. The TGO crack grows towards the TBC/TGO interface as shown in Fig. 11(i) in a similar manner to the initially damage-free models of Fig. 8. Tensile principal stresses, due to CTE mismatch, are observed near the flank of the TGO/TBC interface [Fig. 11 (i)] and this makes the initial TBC crack grow towards the valley. Once the TBC crack reaches the periodicity plane (AB), a rapid separation of the TBC cracked planes occurs according to a linear traction separation law. Principal stress distribution before and after the complete TBC spallation is demonstrated in Fig. 11 (ii). Numerous cracks near the TBC flank after the spallation can be explained by the limitations of Abaqus XFEM enrichment [12]. The elements at the region where those cracks occur have stresses higher than maximum principal stress before spallation. Nevertheless, initiation of cracks is not allowed due to limitation explained in 7.1. After spallation, the damage parameter (STATUSFEM) becomes unity for the existing TBC crack and nucleation of multiple cracks in its vicinity is possible. This results in the spontaneous appearance of multiple cracks at the TBC flank as shown in Fig. 11 (ii) after complete spallation has occurred.

7.4 Influence of initial segmented TBC cracks on crack growth within the TBC system

Fig. 12 shows the maximum principal stresses and cracks within the bulk coating for the system with two initial segmented cracks. When cooling is applied to the system, opening of the initial cracks is not expected to occur. This is because the in-plane (parallel to the TGO interface) mismatch stress within the TBC is compressive due to its lower CTE compared to the BC and substrate. The initial cracks also have no effect on the propagation direction of a TGO crack, which is growing towards the TGO/TBC interface in a similar manner to the damage-free models (Fig. 7). In the vicinity of one of the initial segmented cracks, two parallel cracks are developed during cooling. The propagation of one of the cracks is stalled once it reaches the crack surface of the initial segmented cracks. It can also be observed that if a parallel TBC crack penetrates the TBC/TGO interface, interface separation initiates and the interfacial bond weakens. Normal and effective contact openings at the interface (Fig. 13) significantly increase at the point where TBC crack penetrates the interface ($y/b = 0.72$ in Fig. 13). At that point, the delamination crack is expected to nucleate and this can lead to local separation of the TBC from the substrate.

8 Conclusions

The conclusions made from the presented parametric studies are as follows.

- The thicker the TGO is, the longer the parallel cracks within the TBC and the TGO will be. Coalescence of these cracks within the TBC can lead to partial spallation of the TBC.
- The delamination crack opening at the TGO/TBC interface, as observed from contact openings at the interface, also becomes larger when the TGO becomes thicker.
- In general, tangential contact separations at the TGO/TBC interface are an order of magnitude higher than normal separations. This observation indicates that it is necessary to implement mixed mode interfacial failure.
- Inclusion of initial segmented cracks in the TBC increases the strain tolerance of the TBC and reduces the risk of spallation as the cracks prevent the propagations of parallel cracks. As a result, the lengths of the parallel cracks are significantly shorter for the model with initial segmented cracks (Fig. 12). This confirms that using a spraying method which creates segmented cracks after deposition (e.g. SPPS), is likely to be beneficial for coating life.
- On the other hand, initial parallel micro-cracks within a TBC leads to complete spallation of the TBC and the deposition process has to be optimised to reduce this type of crack.

The proposed algorithm presented can be utilised to predict the failure of TBC systems. However, various sets of data (e.g. fracture toughness and interfacial bond strengths) for mixed-mode fracture behaviour of bulk coatings and interfaces are not currently taken into account due to a lack of experimental data. Moreover, improvements in the XFEM element formulations would enable time dependent creep deformation during steady state to be modelled.

Acknowledgement

We would like to acknowledge the support of The Energy Programme, which is a Research Councils UK cross council initiative led by EPSRC and contributed to by ESRC, NERC, BBSRC and STFC, and specifically the Supergen initiative (Grants GR / S86334 / 01 and EP / F029748) and the following companies; Alstom Power Ltd., Doosan Power, E.ON, National Physical Laboratory, Praxair Surface Technologies Ltd, QinetiQ, Rolls-Royce plc, RWE npower, Siemens Industrial Turbomachinery Ltd. and Tata Steel, for their valuable contributions to the project.

References

- [1] K.W. Schlichting, N.P. Padture, E.H. Jordan, M. Gell, *Materials Science and Engineering A*, 342 (2003) 120-130.
- [2] D. Naumenko, V. Shemet, L. Singheiser, W. Quadackers, *Journal of Materials Science*, 44 (2009) 1687-1703.
- [3] H. Bhatnagar, S. Ghosh, M.E. Walter, *Mechanics of Materials*, 42 (2010) 96-107.
- [4] M. Caliez, J.L. Chaboche, F. Feyel, S. Kruch, *Acta Materialia*, 51 (2003) 1133-1141.
- [5] R. Soullignac, V. Maurel, L. Rémy, A. Köster, *Surface and Coatings Technology*, 237 (2013) 95-104.
- [6] P. Seiler, M. Bäker, J. Rösier, *IOP Conference Series: Materials Science and Engineering*, 10 (2010) 012056.
- [7] T.S. Hille, T.J. Nijdam, A.S.J. Suiker, S. Turteltaub, W.G. Sloof, *Acta Materialia*, 57 (2009) 2624-2630.
- [8] T.S. Hille, A.S.J. Suiker, S. Turteltaub, *Engineering Fracture Mechanics*, 76 (2009) 813-825.
- [9] L. Xie, D. Chen, E.H. Jordan, A. Ozturk, F. Wu, X. Ma, B.M. Cetegen, M. Gell, *Surface & Coatings Technology* 201 ((2006)) 1058-1064.
- [10] U. Hermosilla, University of Nottingham, (Thesis (PhD), 2008).
- [11] V. Maurel, E.P. Busso, J. Frachon, J. Besson, F. N'Guyen, *INT J SOLIDS STRUCT*, 51(19) ((2014)) 3293-3330.
- [12] Abaqus, Dassault Systemes Simulia Corp., (2011).
- [13] C. Sharma, Master Thesis (University of Pavia), (2007).
- [14] M. Martena, D. Botto, P. Fino, S. Sabbadini, M.M. Gola, C. Badini, *Eng. Fail. Anal.*, 13 (2006) 409-426.
- [15] A. Rabiei, A.G. Evans, *Acta Materialia*, 48 (2000) 3963-3976.
- [16] P.K. Wright, A.G. Evans, *Current Opinion in Solid State and Materials Science*, 4 (1999) 255-265.
- [17] M. Bäker, J. Rösler, G. Heinze, *Acta Materialia*, 53 (2005) 469-476.
- [18] T. Belytschko, T. Black, *International Journal for Numerical Methods in Engineering*, 45 ((1999)) 601-620.
- [19] J.M. Melenk, I. Babuska, *Comput. Assist. Mech. Eng. Sci*, 4 (1997) 607-632.
- [20] T. Belytschko, R. Gracie, G. Ventura, *IOP Publishing Ltd • Modelling and Simulation in Materials Science and Engineering*, Volume 17, Number 4, (2009).
- [21] G. Alfano, M.A. Crisfield, *International Journal for Numerical Methods in Engineering*, 50 (2001) 1701-1736.
- [22] S.T. Kyaw, I.A. Jones, T.H. Hyde, *Eng. Fail. Anal.*, 27 (2013) 150-164.
- [23] L. Baiamonte, F. Marra, G. Pulci, J. Tirillò, F. Sarasini, C. Bartuli, T. Valente, *Surface and Coatings Technology*, 277 (2015) 289-298.
- [24] D. Zhu, R. Miller, *Journal of Thermal Spray Technology*, 9 (2000) 175-180.
- [25] V. Lughi, V.K. Tolpygo, D.R. Clarke, *Materials Science and Engineering: A*, 368 (2004) 212-221.

- [26] M.Shinozaki, T.W. Clyne, Presented at Energy Materials Conference, (2012).
- [27] Thompson.J.A, Ji.W, Klocker.T, Clyne T.W, Ninth International Symposium on Superalloys, (2000) 685-692.
- [28] A. Cipitria, I.O. Golosnoy, T.W. Clyne, Sintering Kinetics of Plasma-Sprayed Zirconia TBCs. In, 2007 International Thermal Spray Conference, Beijing, China, 14 - 16 May 2007. ASM International, 434-439.
- [29] E.P. Busso, H.E. Evans, Z.Q. Qian, M.P. Taylor, *Acta Materialia*, 58 (2010) 1242-1251.
- [30] E.P. Busso, J. Lin, S. Sakurai, M. Nakayama, *Acta Mater.*, 49 (2001) 1515-1528.
- [31] E.P. Busso, *J. Phys. IV France*, 09 (1999) Pr9-287-Pr289-296.
- [32] J. Rösler, M. Bäker, K. Aufzug, *Acta Mater.*, 52 (2004) 4809-4817.
- [33] E.P. Busso, Z.Q. Qian, M.P. Taylor, H.E. Evans, *Acta Materialia*, 57 (2009) 2349-2361.
- [34] U. Hermosilla, M.S.A. Karunaratne, I.A. Jones, T.H. Hyde, R.C. Thomson, *Mater. Sci. Eng. A*, 513-514 (2009) 302-310.
- [35] S. Maharjan, X. C. Zhang, F. Z. Xuan, Z. D. Wang, S.T. Tu, *J. Appl. Phys.* 110, 063511 (2011), (2011).
- [36] R.G. Munro, *J. Am. Ceram. Soc.*, 80 (1997) 1919-1928.
- [37] J. Kondoh, H. Shiota, K. Kawachi, T. Nakatani, *Journal of Alloys and Compounds*, 365 (2004) 253-258.
- [38] J.W. Adams, R. Ruh, K.S. Mazdiasni, *Journal of the American Ceramic Society*, 80 (1997) 903-908.
- [39] M. Gell, J. Eric, V. Krishnakumar, K. McCarron, B. Barber, Y.-H. Sohn, V.K. Tolpygo, *Surface and Coatings Technology*, 120–121 (1999) 53-60.
- [40] M. Okazaki, Y. Yamazaki, K. Namba, K. Ogawa, M. Ohki, K. Fujiyama, H. Waki, M. Arai, M. Sekihara, A. Itoh, H. Fukunuma, N. Ohno, H. Kaneko, M. Kawamura, *Journal of Solid Mechanics and Materials Engineering*, Volume 4, Issue 2, pp. 252-263 (2010).
- [41] C. Berndt, *Journal of Materials Engineering*, 11 (1989) 275-282.
- [42] M. Seraffon, N.J. Simms, J.R. Nicholls, J. Sumner, J. Nunn, *Mater. High Temp.*, 28 (2011) 309-314.
- [43] F. Krasucki, S. Lenci, *International Journal of Solids and Structures*, 37 (2000) 3619-3632.
- [44] D.W. Stollberg, J.M. Hampikian, L. Riester, W.B. Carter, *Materials Science and Engineering A*, 359 (2003) 112-118.
- [45] Y.YAMAZAKI, S.KUGA, T.YOSHIDA, *Acta Metallurgica Sinica(English letters)*, Vol.24 (2011) 109-117.
- [46] M. Ranjbar-Far, J. Absi, G. Mariaux, F. Dubois, *Mater. & Des.*, 31 (2010) 772-781.
- [47] The International Nickel Company Inc. Alloy IN-738 technical data.
- [48] C.F.H. Pointer, P. Morrell, Private Communication.

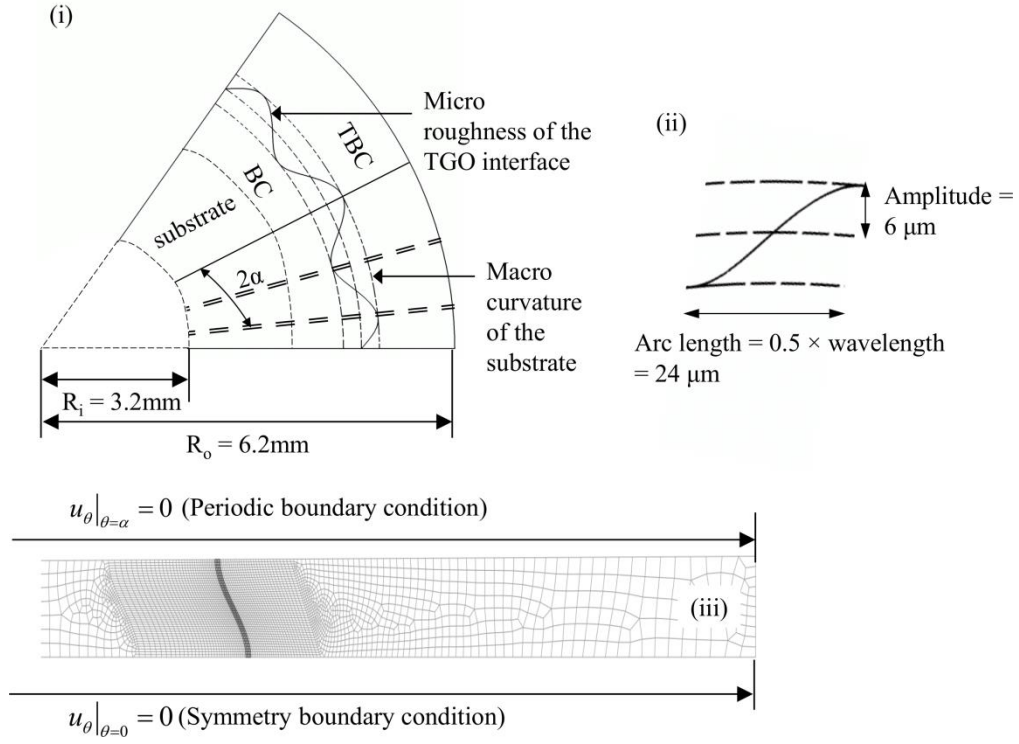


Fig. 1: (i) A TBC system with a sinusoidal TGO with periodicity in the circumferential direction (Cells bounded by double-dashed line are used for a FE unit cell); not to scale (ii) A detailed geometry of the TGO interface (iii) Mesh and boundary conditions of a unit cell (u_θ represents displacement in the circumferential direction))

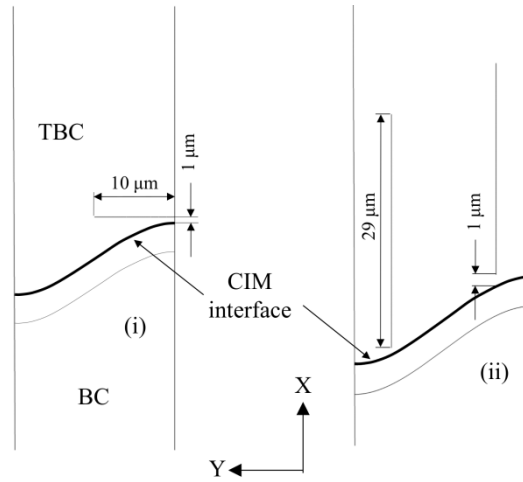


Fig. 2: (i) Parallel and (ii) segmented initial cracks within the TBC

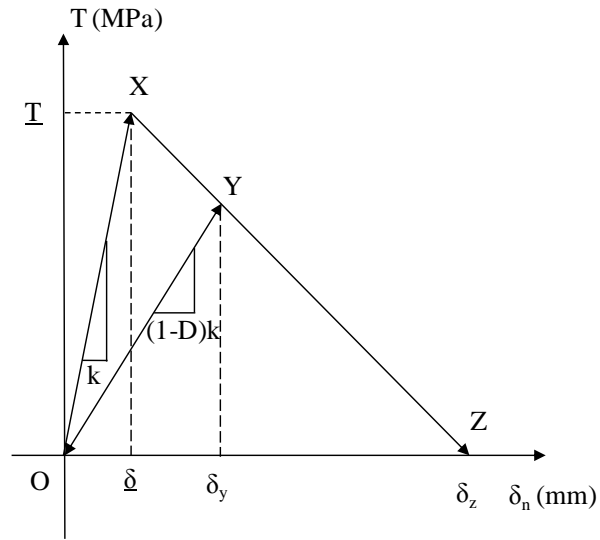


Fig. 3: Linear traction-separation law

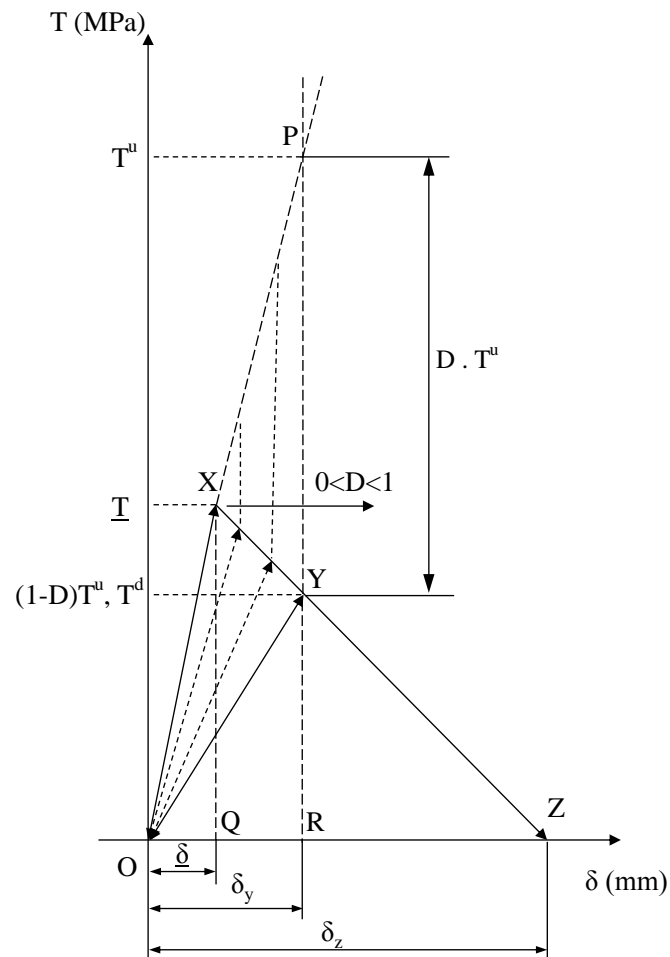


Fig. 4: Damage parameter and unloading process

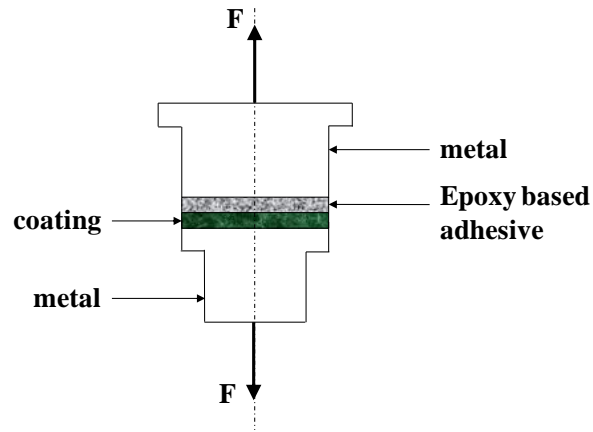


Fig. 5: Adhesion tensile pull test (DIN 50160)

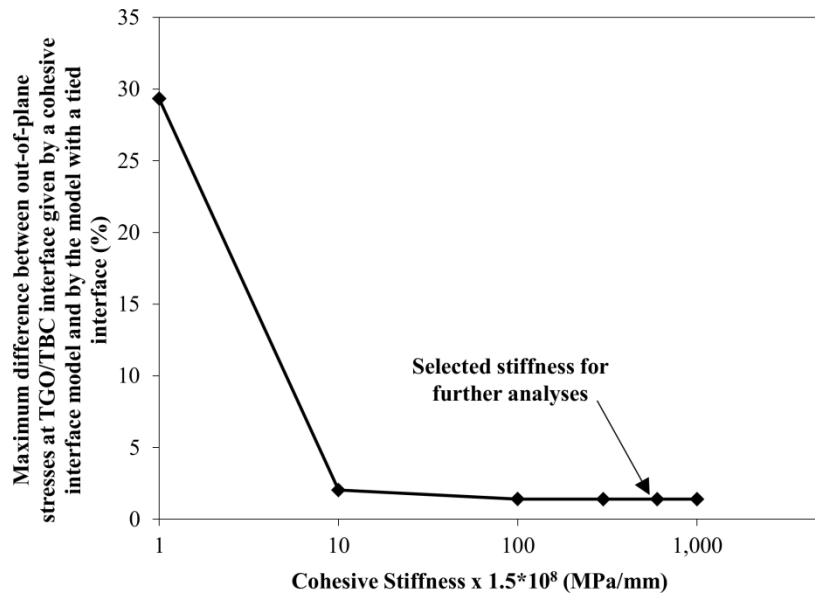


Fig. 6: Maximum difference between out-of-plane stresses at the TGO/TBC interface given by a cohesive interface model with different cohesive stiffness and by the model with a tied interface

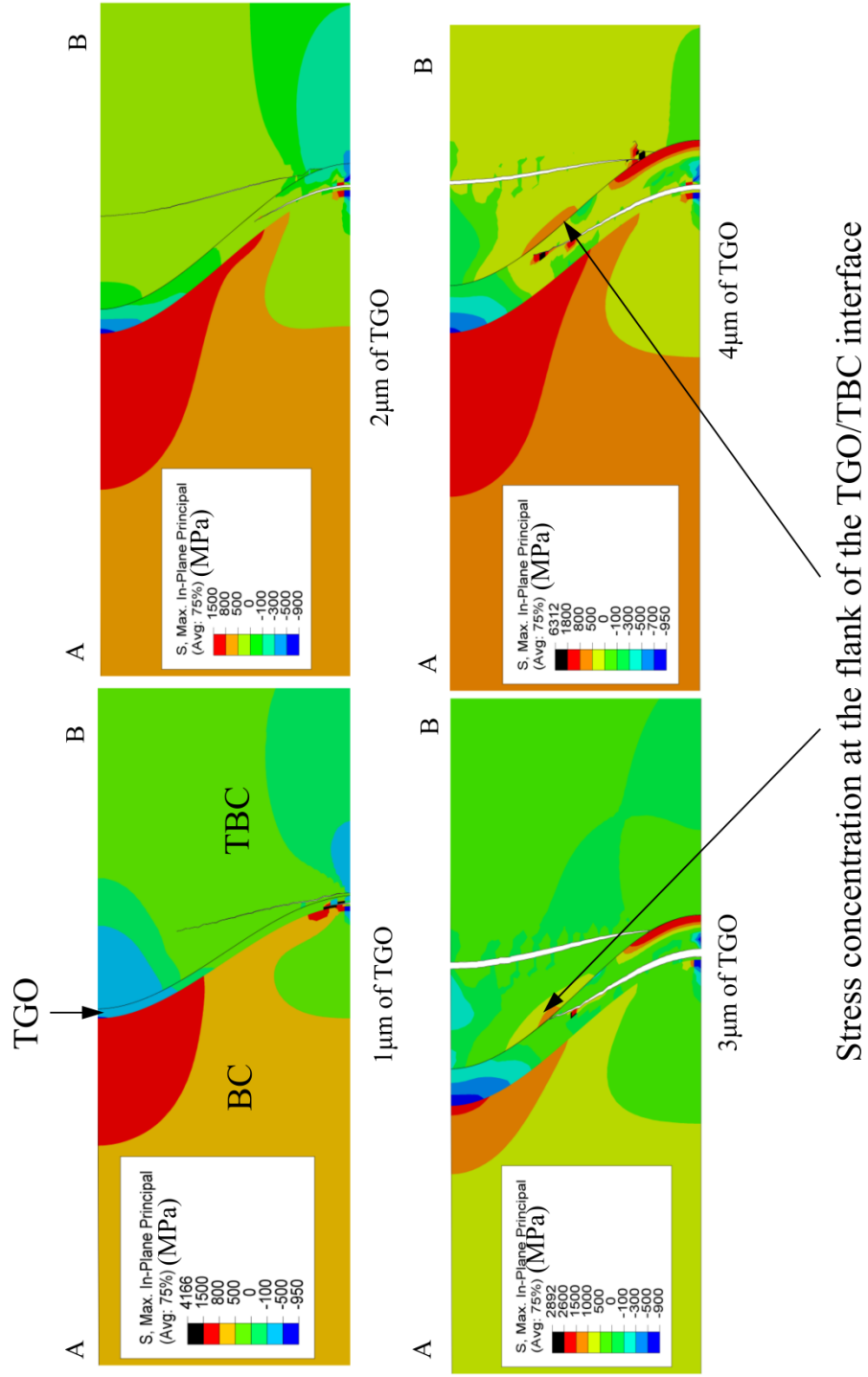


Fig. 7: Maximum principal stresses for the models with different TGO thicknesses

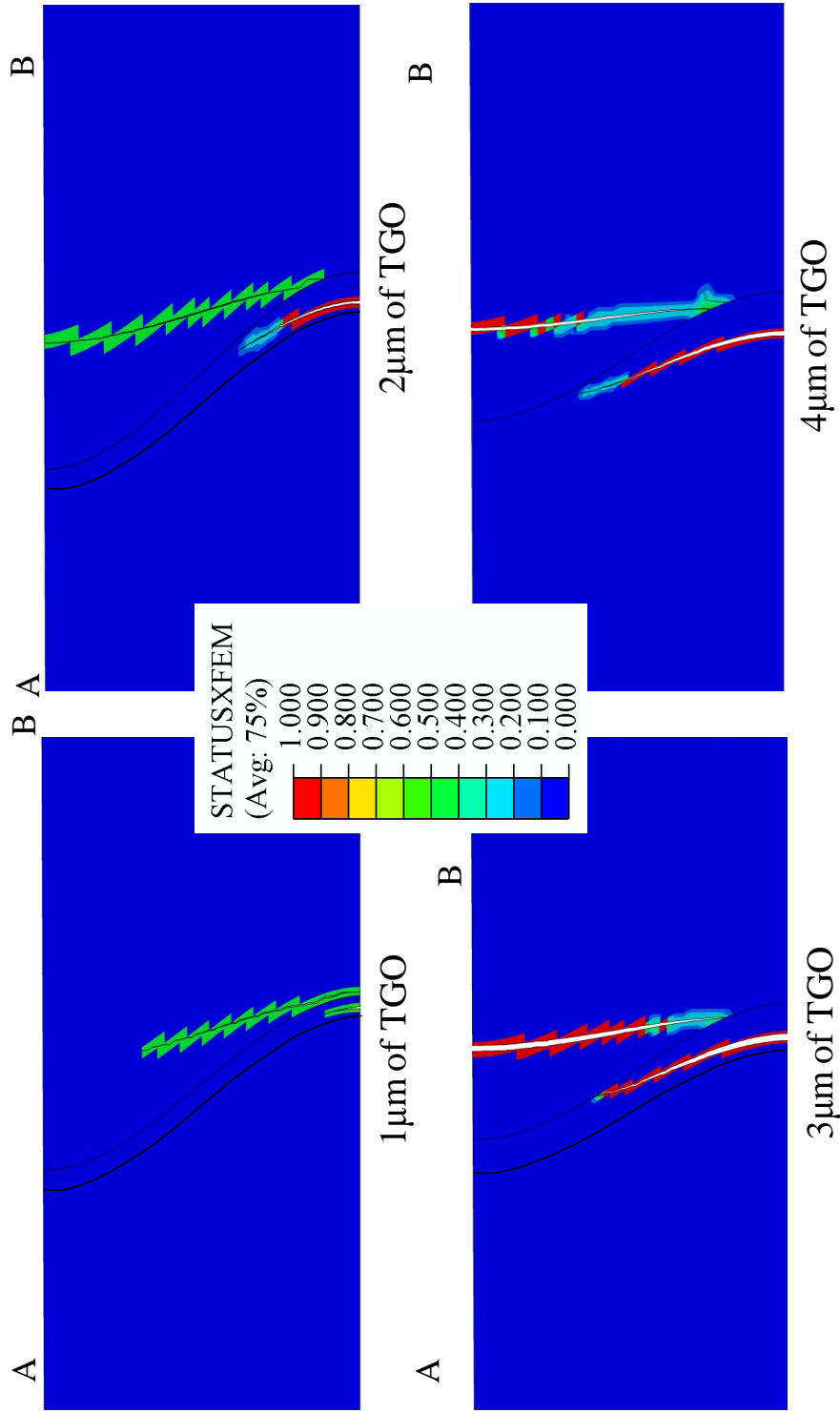


Fig. 8: Status of XFEM elements for the models with different TGO thicknesses (The value is between 1 and 0; 1 means the element is completely cracked with no traction stress across the cracked surfaces)

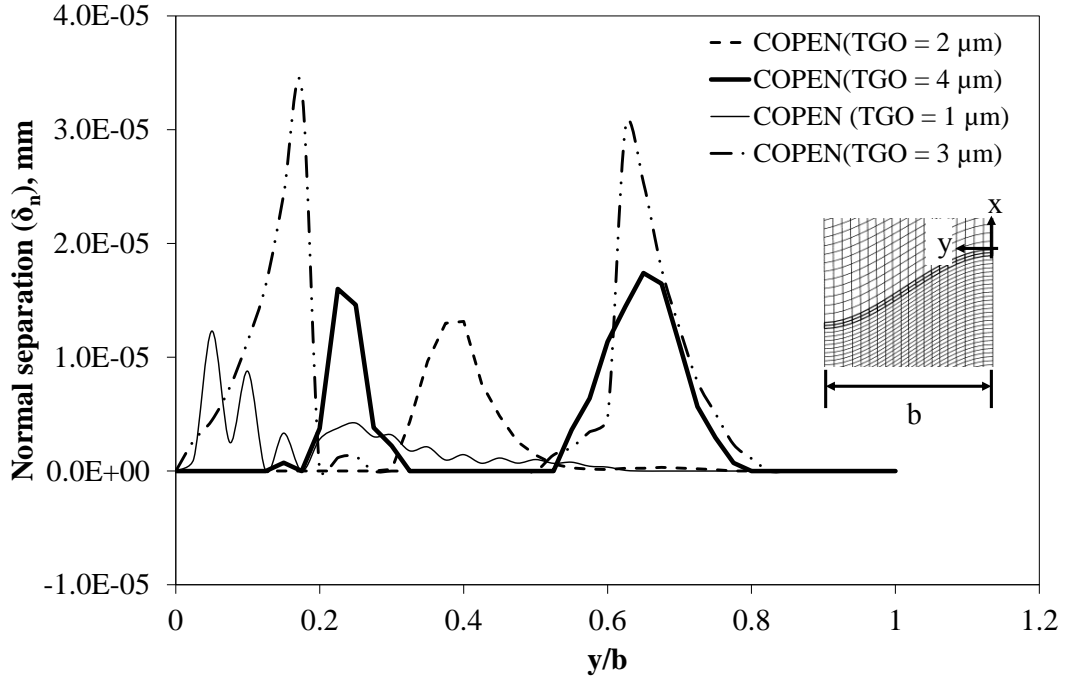


Fig. 9: Normal separations at the TGO/TBC interface for the models with different TGO thicknesses

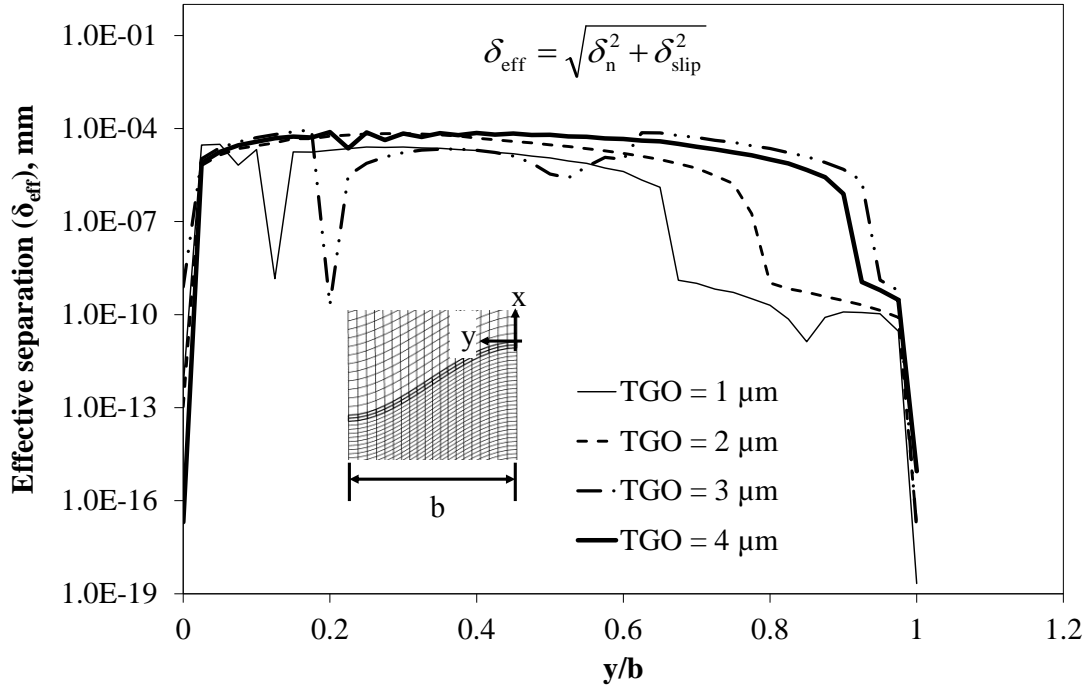


Fig. 10: Effective separations at the TGO/TBC interface for the models with different TGO thicknesses

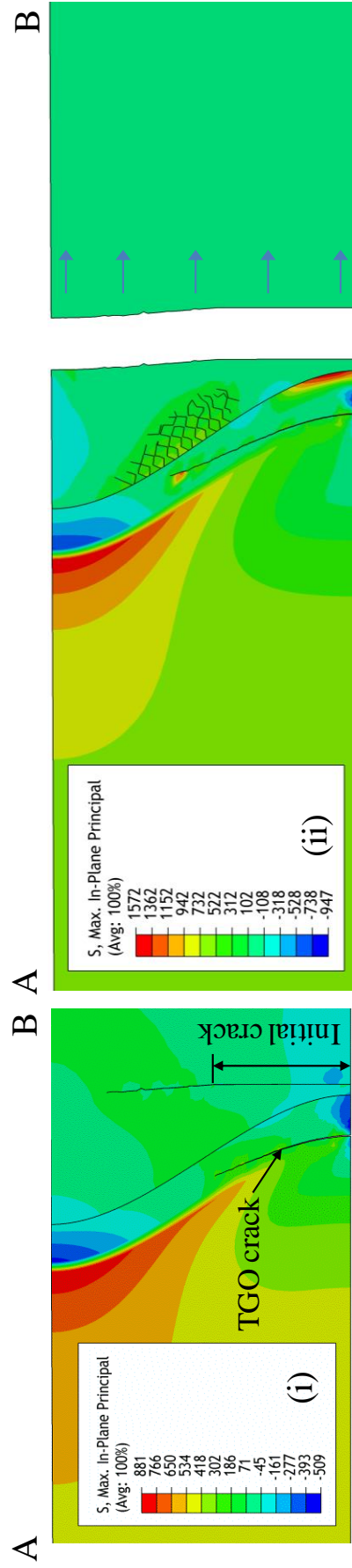


Fig. 11: i) Tensile principal stresses at the tips of growing TBC and TGO cracks ii) complete TBC spallation of the system with an initial parallel TBC crack after cooling to 20°C from 1000°C (4μm TGO)

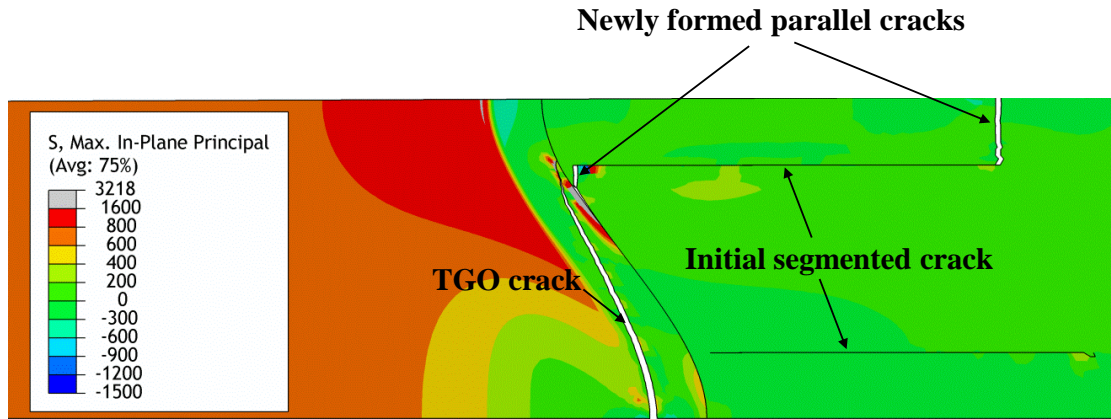


Fig. 12: XFEM cracks within the TBC systems with initial segmented cracks after cooling to 20°C from 1000°C (4μm TGO)

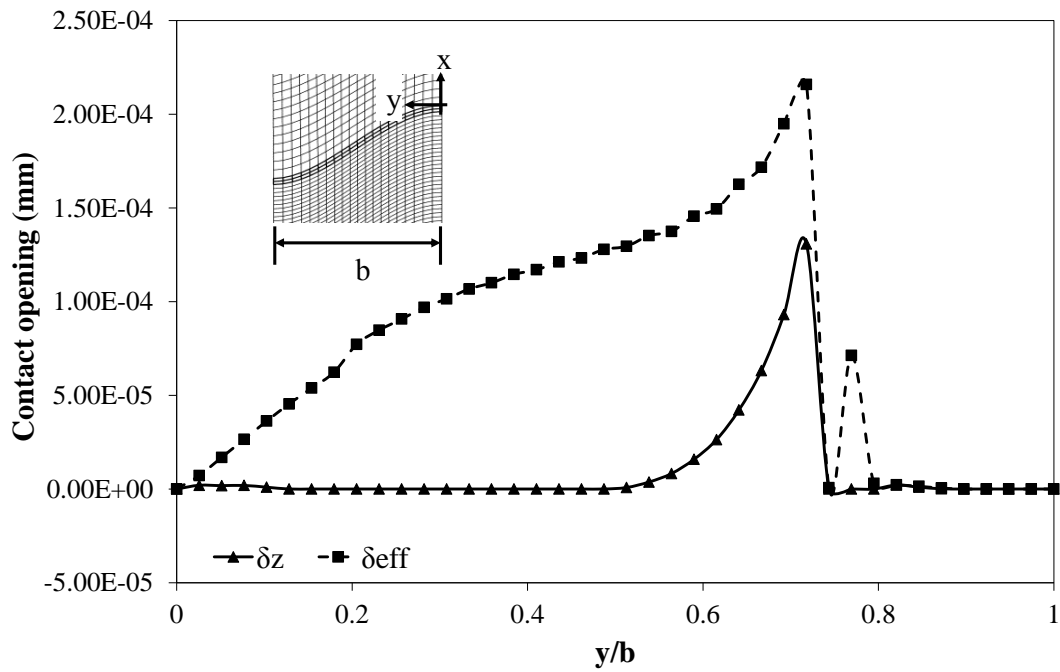


Fig. 13: Normal and effective contact openings at the TGO/TBC interface for the system with initial segmented cracks within the TBC

Table 1: Elastic properties and CTEs of coatings and substrate

Temperature (°C)	Substrate [47]			TBC [24, 48]			TGO [36]			BC [48]		
	E (GPa)	ν	CTE, $K^{-1} \cdot 10^6$	E (GPa)	ν	CTE, $K^{-1} \cdot 10^6$	E (GPa)	ν	CTE, $K^{-1} \cdot 10^6$	E (GPa)	ν	CTE, $K^{-1} \cdot 10^6$
20	-	-	-	120	0.18	10.0	400	0.23	6.62	202.9	0.27	20.
24	206	0.28	11.23	-	-	-	-	-	-			
50	-	-	-	-	-	-	-	-	-	202.7	0.27	50.
93	195.1	0.27	11.97	-	-	-	-	-	-			
200	-	-	-	-	-	-	390	0.23	-	199.92	0.27	200.
204	190.3	0.27	13.23	-	-	-	-	-	-			
316	184.8	0.28	14.4	-	-	-	-	-	-			
400	-	-	-	-	-	-	380	0.24	-			
500	-	-	-	-	-	-	-	-	-	184.8	0.27	500.
538	175.1	0.3	16.2	-	-	-	-	-	-			
600	-	-	-	-	-	-	370	0.24	-			
700	-	-	-	-	-	-	-	-	-	167.72	0.27	700.
760	157	0.3	-	-	-	-	-	-	-			
800	-	-	18.38	-	-	-	355	0.25	-			
871	151	0.29	-	-	-	-	-	-	-			
982	140	0.3	19.42	-	-	-	-	-	-			
1000	-	-	-	-	-	-	325	0.25	-	131.6	0.27	1000.
1200	-	-	-	-	-	-	-	-	8.7	100.52	0.27	1200.